ASME Journal of Engineering for Gas Turbines and Power
Online journal at:
https://asmedigitalcollection.asme.org/gasturbinespower

A Study on Combustion Characteristics of Radial Inward Flow Porous Media Burners for Ammonia-Hydrogen Flames

Guguloth Mahesh Nayak
Faculty of Aerospace Engineering,
Technion – Israel Institute of Technology,
Haifa, Lady Davis 380,
Haifa 3200003, Israel
e-mail: gmaheshnayak@campus.technion.ac.il

Beni Cukurel[1]
Faculty of Aerospace Engineering,
Technion – Israel Institute of Technology,
Haifa, Lady Davis 740,
Haifa 3200003, Israel
e-mail: beni@cukurel.org

Joseph K. Lefkowitz[1]
Faculty of Aerospace Engineering,
Technion – Israel Institute of Technology,
Haifa, Lady Davis 380,
Haifa 3200003, Israel
e-mail: joseph.lef@technion.ac.il

The present study investigates the potential of porous media burners to enhance the combustion characteristics of ammonia (NH_3), attributable to the structure's heat recirculation, which extends the flammability limits of premixed flames. This study establishes a radial inward flow porous media burner with dynamic flame stabilization, featuring a compact ceramic foam made of silicon carbide. The foam's Voronoi-based lattice porous structure includes a continuously graded topology, with a linear void fraction increasing from the outer to inner radial direction. The burner flammability limits were evaluated with up to 30% hydrogen (H_2) by volume added to the fuel stream. The stability range for pure NH_3 operation was $0.8 \leq \phi \leq 1.3$, which was extended to $0.55 \leq \phi \leq 1.5$ for 30/70 H_2/NH_3 mixtures. Revealing the flame front propagation behavior under various operating conditions, infrared radiometry was employed to determine the solid matrix temperature using a narrow bandpass filter to avoid interference from gaseous species. The exhaust gas and ceramic foam temperatures were correlated to provide insight into flame dynamics. Emissions of NO, N_2O, along with NH_3 and H_2 slip, were analyzed for various mixture compositions and equivalence ratios. Conditions which minimized NO emissions included (a) near lean-limit NH_3/H_2 combustion, (b) rich conditions of $\phi \geq 1.2$, and (c) pure NH_3 at near-stoichiometric conditions with low combustion temperature due to low mass flux. The measured pollutant emissions were compared with a perfectly stirred reactor model, yielding good agreement. [DOI: 10.1115/1.4069447]

Keywords: porous media burners, ammonia combustion, radial-inflow burner, flame stabilization, combustion efficiency, emissions, hydrogen enrichment, matrix stabilized combustion, infrared imaging radiometry, compact combustor design, heat recirculation, micro gas turbines

1 Introduction

The consumption of fossil fuels contributes significantly to pollution and climate change, necessitating carbon reduction strategies [1]. Therefore, an alternative fuel to mitigate the impact of global warming, ammonia (NH_3), has emerged as a promising future carbon-free fuel due to the large-scale existing infrastructure for its production, distribution, and storage as well as the associated technical expertise [2,3]. Ammonia contains 17.8% H_2 by mass, coupled with easier and more cost-effective storage and transport capabilities compared to H_2, presents itself as a promising sustainable option as an energy vector for transportation, power generation, and heavy industry [4–8]. However, NH_3 produces high concentrations of emissions NO_x, N_2O, and unburned NH_3 in the exhaust [4,9]. In addition, NH_3 exhibits poor combustion characteristics such as low flame speed, reduced heating value, long ignition delay, and large flame thickness compared to traditional hydrocarbon fuels [4,10–13].

Numerous studies have investigated the combustion characteristics of NH_3 flames under a range of operating conditions using various swirl stabilization-configured test rigs [14–17]. A frequent strategy used in these studies to improve the combustion properties of NH_3 is the addition of more reactive fuels such as hydrogen, methane, synthesis gas, or diesel fuel. In particular, the stability limits of combustor operation using NH_3/H_2 mixtures have been widely reported over a range of NH_3/H_2 fractions, equivalence ratios (ϕ), operating pressure, and with the addition of steam [14,17–20]. The stability limits of pure NH_3 flames and mixtures of NH_3/H_2 flames are dependent on burner geometry, with a single configuration only able to optimize stabilization limits over a narrow range of mixtures [16]. To utilize a wide range of mixtures, a burner design with extended flame stability limits compared to swirl-stabilized geometries is desirable.

A recent comprehensive review focused on flame stabilization and nitrogen-containing pollutant emissions from NH_3 and NH_3/H_2

Turbo Expo: Turbomachinery Technical Conference & Exposition (GT2025) June 16–20, 2025. GT2025.
[1]Corresponding authors.
Manuscript received July 1, 2025; final manuscript received July 17, 2025; published online September 24, 2025. Editor: Jerzy T. Sawicki.

combustion, including NO, N_2O, NO_2, and unburned NH_3 [19]. Studies found that NO emissions are lowest under very lean ($\phi \leq 0.7$) or rich ($\phi \geq 1.2$) conditions, and peaked near the equivalence ratio range of $0.75 \leq \phi \leq 0.90$, exhibiting emissions over 4500 ppm [17,21–23]. Fuel-rich conditions produce unburned NH_3 and H_2, necessitating second-stage combustion to maintain high efficiency. Modern gas turbine engines typically operate under very lean combustion conditions ($\phi \leq 0.6$), which results in low NO emissions [24]. Unfortunately, for NH_3, these conditions result in increased pollutants such as N_2O, unburned NH_3 emissions, and combustion efficiency becomes an issue [24–26]. To overcome these challenges, advanced combustor concepts have been explored. A review of NO_x mitigation strategies reported for fuel-rich combustion, high-pressure combustion, reactant humidification, plasma-assisted combustion, and staged combustion found various degrees of pollutant mitigation [23]. However, these methods face challenges of difficulty in operation, effectiveness under limited conditions, and engineering complexity, necessitating continued research.

Porous media combustion has emerged as a promising approach to widen stability limits compared to swirl-stabilized combustors, particularly for unconventional fuels, fuels with low heating values, or operation with ultralean mixtures [27,28]. The unique characteristics of porous media burners (PMBs) lie in their ability to recirculate heat through thermally conductive ceramic matrices, enhancing flame stability by preheating incoming reactants and extending flammable limits. This results in super-adiabatic combustion, enabling operation under lean conditions and potentially increased thermal loads [29]. The configuration of PMBs, including material properties such as pore density and thermal conductivity, plays a significant role in stabilizing flames and mitigating emissions [27,28,30,31].

Previous investigations demonstrated the difficulty of stabilizing pure ammonia flames in PMBs. Single-layer ceramic foams with uniform pore densities provided limited stabilization due to incomplete combustion and insufficient heat recirculation [32]. Multilayer PMB designs were subsequently introduced to overcome these challenges. Studies utilizing porous ceramic foams with different pore densities, such as transitions between 40 pores per inch (PPI) to 3 PPI or 10 PPI (finer to coarser structures), demonstrated enhanced flame stabilization and pollutant emission control for ammonia, ammonia-hydrogen and ammonia-methane mixtures and the findings highlighted that the transitions at foam interfaces anchor the flame at a particular location [33–35]. Moreover, higher thermal conductivity and denser pore structures were shown to reduce peak temperatures and facilitate stabilization by preventing flashback while providing efficient preheating [36,37]. A following study introduced a two-stage porous media burner in a rich-quench-lean configuration to address the limitations of single-stage configurations, particularly concerning pollutant emissions [38]. The PMB burner design, in the stream-wise direction, is as follows: first stage: two YZA 40 PPI - SiC 3 PPI- SiC 10 PPI, and follows the second stage: SiC 3 PPI- SiC 10 PPI- SiC 20 PPI, including air injection. The graded structure allows coarse foam layers to prevent flame quenching, while finer layers reduce the risk of flashback. The two-stage configuration demonstrated substantial reductions in nitrogen oxide and unburned ammonia emissions compared to single-stage designs.

Efforts to date on porous media burners with axial flow configurations have made significant progress, achieving pure ammonia combustion within a wide range of equivalence ratios and flow rates. Two-stage configurations have demonstrated low NO_x operation while maintaining high combustion efficiency. However, these designs rely on multilayer ceramic foams, which increase burner size and pressure losses, limiting their applicability in microgas turbine engines [39,40]. Initially designed for an ultra-microgas turbine application [41], the present work introduces an alternate geometric configuration of radially inward flow PMB. To evaluate this configuration, a graded silicon carbide Voronoi-based lattice porous structure with a linear pore density is used to stabilize ammonia-hydrogen-air flames. Experimental and numerical methods assess flame stabilization and pollutant emissions across 0–30% hydrogen in ammonia mixtures and equivalence ratios of $0.6 \leq \phi \leq 1.5$. Infrared imaging radiometry measures the ceramic foam temperature distribution, and a perfectly stirred reactor model analyzes emissions under lean and rich conditions.

2 Experimental Method

The experimental setup for this study utilized a lab-scale radial inward flow porous media burner, designed to facilitate, control, and monitor combustion parameters. The schematic of the experimental setup is shown in Fig. 1(*a*). The reactant mixture, composed of NH_3, H_2, and air, was controlled using an array of mass flow controllers (Alicat MCR-250 SLPM, MCS-50 SLPM, Bronkhorst F201CV). Thermocouples were placed across the burner to monitor the temperature of the inlet mixture (T_{inlet}, K-type), the burner operating temperature (T_{burner}, K-type), and the exhaust gas temperature (T_g, R-type). The burner operating temperature T_{burner} was kept at $400 \pm 20^{\circ}$ to ensure the combustion thermal conditions remained similar to account for changes in the fuel mixture and flow rates. Thermal stabilization was defined by maintaining the exhaust temperature within a $\pm 5\,^{\circ}\text{C}$ range, with deviations indicating flame behaviors such as extinction or flashback. The combustion products exit the burner through the exhaust, as shown in Fig. 1(*a*), where a gas analyzer (Testo-340) was incorporated to characterize the emission of NO (± 5–10%) and the residual of O_2 ($\pm 0.75\%$). N_2O and unburned NH_3 ($\pm 5\%$) were measured by Fourier transform infrared spectroscopy and H_2 ($\pm 5\%$) by gas chromatography (GC). The experiments were conducted at ambient temperature and pressure. An NI cDAQ control system was used to instrument the experimental setup.

Figure 1(*b*) illustrates the construction of the radial inward flow configuration in the burner cross section. The ceramic foam block in the PMB is supported by a central solid cone body that channels the premixed reactant mixture into the porous media. The foam is configured to receive the mixture at the outer circumference, directing the flow radially inward toward the hollow core before expulsion through the burner exhaust. A spark plug is located adjacent to the solid matrix region to ignite the reactant mixture. The thermocouple measuring the exhaust gas temperature (T_g) is located immediately downstream of the combustion products that exit the porous structure. In addition, an optical window enabled the visualization of the combustion itself, covering approximately 2/3rd of the porous inert media (PIM) radius. A midwave (1.5–5.4 μm) infrared camera (FAST M3k-TELOPS) equipped with a bandpass filter at a wavelength of 2085 ± 10 nm is used for infrared imaging radiometry. The infrared data was utilized to estimate the solid matrix temperature of the foam (T_s), covering a radial distance of 16.5 mm for a total of 21 mm PIM. Infrared images were acquired using a specific filter targeting a null spectral region, ensuring that only the surface emission from the ceramic foam was captured, while emissions from gaseous species within the solid matrix were excluded. The infrared radiometry procedure is detailed in Ref. [42]. For the temperature estimation, the emissivity (ε) of the foam SiC was assumed to be approximately 0.90 [37]. Previous studies have reported emissivity values for SiC in the range of 0.85–0.95, reflecting its temperature-dependent emissivity in a broad spectral region [43–46]. The resultant estimated ceramic temperature T_s ranges from 1100 to 1450 K with an uncertainty of 5%, primarily attributed to the temperature-dependent transmissivity of the sapphire window ($\pm 5\%$) and the potential deviations from the assumed SiC emissivity (± 0.05).

The ceramic foam block used in the current PMB has a thickness (L) of 21 ± 1 mm, with an outer diameter of 60 ± 1 mm and an inner diameter of 18 ± 1 mm. The foam material is made of SiC, which has a high thermal conductivity (20–50 W/m.K at $1000\,^{\circ}\text{C}$) and good thermal shock resistance (230 K) [47]. The foam features a linearly graded lattice structure with a pore void fraction varying from 60% to 90% from the outer circumference to the radially inward

direction. An image of the PIM structure is portrayed in Fig. 1(*c*). The porous media used in this study is based on a Voronoi lattice structure, which provides a mathematically defined partitioning of space that accurately captures irregular pore distributions. In this case, seed points are placed in the three-dimensional space in a graded manner such that the void fraction of the pores increases in the radial inward direction. Then the lattice is generated by forming regions (or cells) consisting of all points in space closest to a specific seed point [48]. In the present burner, the irregularity of the seed points facilitates an easily controlled variation in void fraction from the outer to the inner surface of the annular solid matrix.

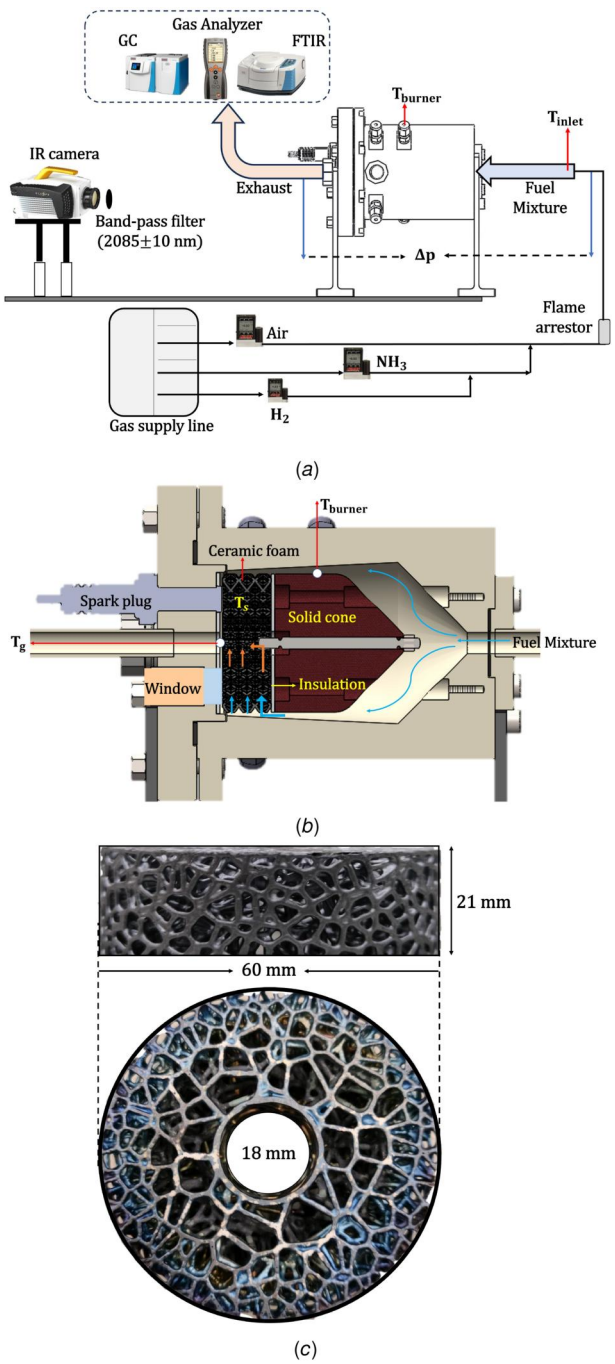

Fig. 1 (*a*) Schematic of the experimental setup including premixed gas supply, line of sight infrared measurements, and downstream composition analysis system, (*b*) cross-sectional view of the combustor portraying the gas path across the PMB and the observation window, and (*c*) the lattice Voronoi structure of the porous inert media in side and top views

In order to characterize the nominal velocity field inside the porous structure with radial inward gas path, cold flow Reynolds-averaged Navier-Stokes simulations were conducted using ANSYS Fluent. The computational domain used in the numerical simulation mimics the experimental test rig and its flow conditions. In the absence of chemical reactions, Fig. 2 portrays the velocity distribution for mass flux $\dot{m}'' = 0.19\,\mathrm{kgm^{-2}s^{-1}}$. The porous structure is designed with a varying void fraction along the radial direction, which modifies the local flow distribution and thus controls the velocity field. At the outer surface of the cylinder, a lower void fraction results in greater solid matrix presence, effectively regulating the fluid passage and creating localized regions of higher velocity. As the flow progresses inward, the gradual increase in void fraction reduces the obstruction to flow, leading to a decrease in velocity at a certain radial location. Beyond this region, velocity is augmented due to the reduced flow area in order to maintain mass continuity at reduced radius.

Then, the data are postprocessed, where the circumferentially averaged velocity profile is computed to compare flow distribution at different axial positions (z). Obtained by averaging data across six radial probe lines at fixed radii and further normalized using geometric cold flow velocity based on the inner gross area for the given mass flowrate, Fig. 3 presents the normalized velocity across the radial direction at different positions (z) across the foam thickness (L), illustrating the flow distribution within the porous structure.

A localized region of higher velocity was realized on the outer surface, followed by a gradual increase in void fraction, which leads to a drop in velocity at a certain radial position (depending on the axial plane), and further downstream, the velocity increases once again due to the reduction in area. Therefore, as the mixture travels through the porous media, the flame tends to stabilize at a location where the kinematic balance between the burning velocity and the fresh mixture velocity is achieved. It should be noted that the flow is highly turbulent and the lattice structures create local recirculation zones, but nevertheless, the residence time is still expected to be inversely proportional to the local mean velocity. An additional trend is seen in the axial direction from $z/L = 0$–1, where the flow velocity at the outer diameter gradually decreases with z, while the flow at the inner diameter gradually increases. This leads to a secondary stabilization location, which is observed for high x_{H_2}

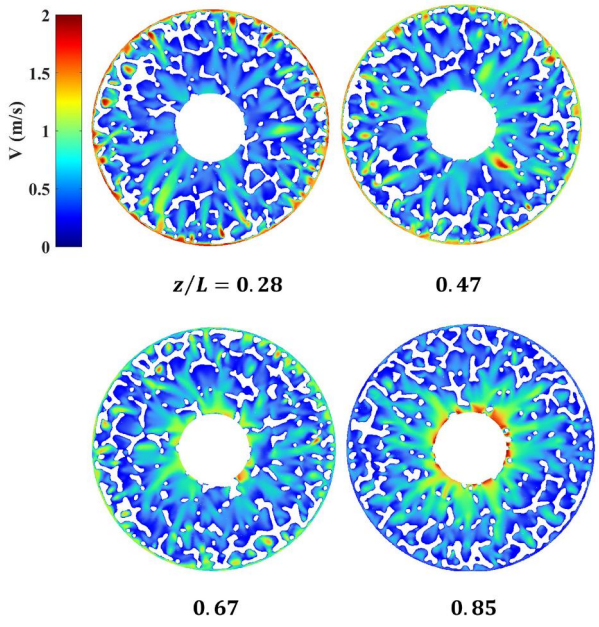

Fig. 2 Velocity contour inside the porous structures at different positions (z) across foam thickness (L) for mass flux of $\dot{m}''$=0.19 $\mathrm{kgm^{-2}s^{-1}}$, axial direction is from z/L = 0–1

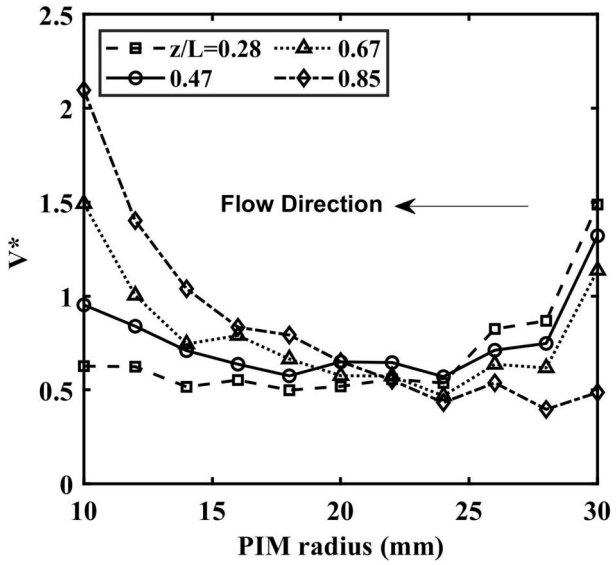

Fig. 3 The circumferential averaged velocity profile (normalized by the geometric cold flow velocity from the inner gross area) along the radial direction at different axial locations (*z*) across the foam thickness (*L*), from cold-flow simulations

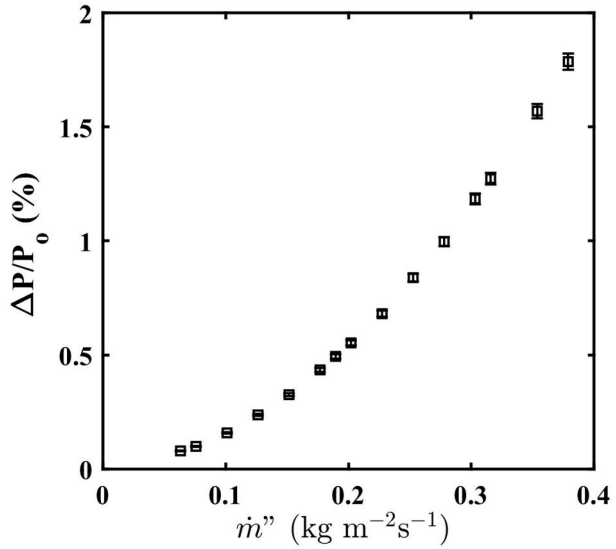

Fig. 4 Experimental pressure drop across the porous media burner at atmospheric exit conditions

fractions in the fuel mixture. It is acknowledged that the presence of combustion and upstream conduction will increase velocity augmentation in the radial inward direction, driven by the local drop in gas density, resulting in thermal expansion that further accelerates the flow. Furthermore, the pressure drop ($\Delta P/P_o$) across the porous burner under cold-flow conditions of air is found to be approximately 1.8% for the highest mass flux conditions considered in this study, as shown in Fig. 4.

3 Results and Discussion

3.1 Burner Flame Stability. This section examines the stability limits of the radial PMB by examining three key parameters: reactant mass flux ($\dot{m}''$, mass flowrate per unit surface area of the outer cylindrical surface of the foam), equivalence ratio (ϕ) and volumetric ratio of NH_3 to H_2 in the fuel mixture, represented by volume fractions x_{NH_3} and x_{H_2}, with condition $x_{NH_3} + x_{H_2} = 100\%$. Following a systematic investigation, the burner stability map was created, as presented in Fig. 5. The shaded blue region indicates a stable operating condition, while the other boundary represents extinction. The study excluded unshaded regions (white) where experiments were not performed due to burner limitations or safety concerns.

For pure NH_3 (Fig. 5(*a*)), stable flame operation was achieved across an equivalence ratio range of $0.8 \leq \phi \leq 1.3$ at $\dot{m}'' = 0.12$ $\text{kgm}^{-2}\text{s}^{-1}$. As the mass flux increased to 0.25 $\text{kgm}^{-2}\text{s}^{-1}$, the stability range narrowed to $0.9 \leq \phi \leq 1.1$, with the flame remaining anchored without extinction risk. This represents the first instance of a radial inward-flow PMB effectively stabilizing pure NH_3 flames. The graded porous media, combined with the radially inward flow configuration, stabilized the flame by creating a velocity gradient in which the flame speed dynamically matched the local velocity over a range of mass flux and flame speed conditions. The heat recirculation through the ceramic matrix and large pore size promoted a high burning velocity and sufficient thermal thickness to prevent quenching of the ammonia flame [35,38]. These stability limits are comparable to those of multilayered porous media burners reported in earlier studies in terms of the equivalence ratio range [35], although the mass flux range is relatively limited.

Introducing 10% H_2 into the fuel mixture (Fig. 5(*b*)) significantly extended the burner's stability, allowing it to handle up to 50% higher mass flux compared to pure NH_3. At $\dot{m}'' = 0.12\,\text{kgm}^{-2}\text{s}^{-1}$, the equivalence ratio range expanded to $0.7 \leq \phi \leq 1.5$. For near-stoichiometric mixtures the maximum mass flux was extended to $\dot{m}'' = 0.38\ \text{kgm}^{-2}\text{s}^{-1}$, enabling broader operational flexibility. Note that this does not represent the upper limit of mass flux attainable, but above this condition, the burner temperature exceeded safe operating conditions.

Further increasing the H_2 content to 20% (Fig. 5(*c*)) continued to extend stability improvements, reducing the lean extinction limit to $\phi = 0.6$, and operating without flashback across all equivalence ratio and mass flux conditions attempted. Comparing all of the cases, the addition of H_2 consistently broadened the stability range, particularly under lean conditions. While pure NH_3 combustion required narrow equivalence ratios at higher mass flux, the enriched mixtures enabled extended operational flexibility. However, this stability enhancement has limits as the H_2 content is further increased: flashback was observed at higher H_2 concentrations, occurring at $x_{H_2} = 40\%$ and 50% for $\dot{m}'' = 0.12$ and $0.19\ \text{kgm}^{-2}\text{s}^{-1}$, respectively. These results emphasize the compromise between mass flux, equivalence ratio, and H_2 enrichment in optimizing burner performance.

The turndown ratio, a critical performance metric for enabling flexible operation under diverse conditions in industrial combustion systems, was significantly enhanced by porous media configurations. These configurations support higher mass fluxes than conventional burners, such as Riello burners designed for hydrocarbon fuels, thereby improving premixed combustion performance [35]. In the present PMB configuration, the exhaust pipe temperature imposed restrictions on the mass flux range, limiting a comprehensive exploration of the turndown ratio. However, the introduction of 20% H_2 demonstrated a promising enhancement of the turndown ratio. Building on this, the thermal power density ($\dot{q}_v$) was evaluated under stabilized mass flux conditions, defined as the thermal power output per unit volume of the combustion zone. Maximizing $\dot{q}_v$ enables higher energy outputs relative to system size. A comparison of $\dot{q}_v$ among conventional PMBs (three-layered), our PMB, and swirl-stabilized flames operating under ideal stoichiometric conditions of pure NH_3 at atmospheric pressure is presented in Fig. 6. At similar mass fluxes used in this study, the power density of the PMB is higher than that of the three-layered PMB [35]. Notably, this value significantly exceeds the power density observed in swirl-stabilized flames, which ranges between 5 and 22 MW/m^3 [22,35,49]. Furthermore, adding 20% H_2 to the fuel mixture increased the power density by a factor of 2.75, emphasizing the impact of H_2 enrichment on system performance.

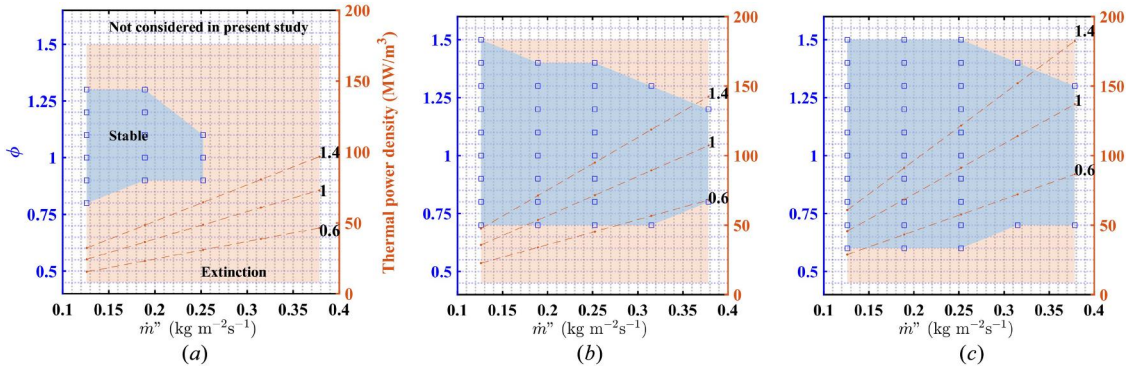

Fig. 5 Burner stability map as a function of equivalence ratio ϕ and mass flux $\dot{m}''$ for various volumetric compositions of the fuel mixture, x_{NH_3}. Experimental condition points are represented in the shaded region (squares). Dashed lines correspond to thermal power density for ϕ=0.6, 1, and 1.4. (*a*) x_{NH_3} = 100%, (*b*) x_{NH_3} = 90%, and (*c*) x_{NH_3} = 80%.

3.2 Solid Matrix Temperature (T_s). Providing an insight into the burner's flame stabilization characteristics, the temperature distribution across the solid matrix was estimated (Fig. 7(*a*)) for a range of equivalence ratios at constant mass flowrate and pure ammonia combustion, (Fig. 7(*b*)) for a range of mixture compositions at constant mass flowrate and stoichiometric combustion, and (Fig. 7(*c*)) for a range of mass flow rates at constant stoichiometric pure ammonia combustion. The reactant mixture flowing radially inward is indicated by the right to left pointing arrow direction. Accordingly, the right side of the window represents the upstream region (approximate radius 28 mm), and the left corresponds to the downstream (13 mm), depicted in Fig. 7(*a*). Moreover, the radial profile of the average solid temperature T_s along the centerline and the measured exhaust gas temperature T_g are presented in Fig. 8.

For a range of ϕ values, the solid matrix temperature distribution of NH_3/air flames is shown in Fig. 8(*a*) at a constant mass flux of $\dot{m}'' = 0.19\,\mathrm{kgm^{-2}s^{-1}}$. The maximum T_s observed under these conditions is approximately 1350 K, which sets the location of the flame front near 16 mm since the peak T_s region generally aligns with the flame front [37]. The temperature gradient of T_s upstream of the maximum point indicates the flame front propagation inside of the porous media, with dynamic stabilization dependent only on the geometry of the PMB. Variations in the temperature of the preheat zone provide insight into the stabilization points for different equivalence ratios (ϕ). For near stoichiometric conditions (ϕ = 1, 1.1, and 1.2), the flame is located at the same radial position and follows a similar upstream gradient. It is notable that, despite the differences in the adiabatic flame temperatures, which would be present in a normal combustor, the temperature profile for these three mixtures is nearly identical. This indicates the impact of heat recirculation, which largely controls the thermal profile of the burner within this equivalence ratio range. A steeper T_s gradient is observed in the leaner (ϕ = 0.9) and richer mixtures (ϕ = 1.3), the latter is consistent with prior observations in literature [12]. Despite these distinct behaviors in flame stabilization for different equivalence ratios, the exhaust temperature (T_g) remains similar under all conditions. It suggests that while the internal temperature gradients within the ceramic structure vary significantly with ϕ, dictating a changing flame position and relative radiation heat losses, the exhaust temperature was comparable for all cases. The radiative heat loss fraction under these conditions is estimated to be approximately 10%, and a more detailed discussion on the subject is provided in Appendix A.

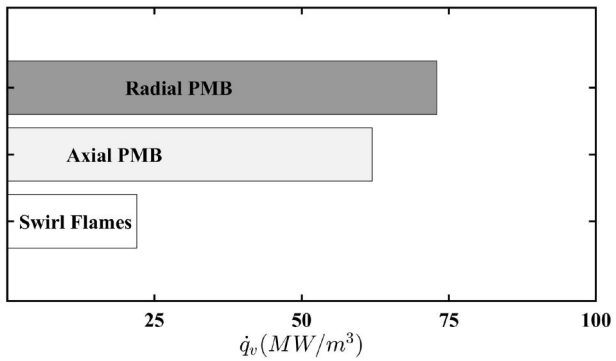

Fig. 6 A comparison of thermal power density for different combustion configurations of NH_3 flames

Under stoichiometric conditions for mass flux of $\dot{m}'' = 0.19$ $\mathrm{kgm^{-2}s^{-1}}$, Fig. 8(*b*) illustrates the effect of NH_3/H_2 mixture composition, varying from x_{NH_3} = 100–70%. The temperature distribution progressively shifts upstream (reducing the preheating zone), with the high-temperature region becoming more compact and localized. The most pronounced upstream stabilization is observed for $x_{NH_3} = 70\%$, as indicated by a lower upstream T_s compared to $x_{NH_3} = 80\%$ and $x_{NH_3} = 90\%$ cases, indicating that the flame is stabilized significantly upstream of the viewing window. This is attributed to the higher reactivity and flame propagation speed of H_2. Upstream flame stabilization affects the thermal distribution within the porous media by diminishing the preheating zone while increasing heat loss to the postcombustion zone, reducing the porous media to a flame holder. In addition, the exhaust temperature T_g is found to be strongly influenced by the mixture concentration, where the highest values were observed for pure NH_3 combustion.

Figure 8(*c*) demonstrates the effect of mass flux on flame stabilization while maintaining a stoichiometric equivalence ratio for pure ammonia. At a mass flux of $\dot{m}'' = 0.12$ $\mathrm{kgm^{-2}s^{-1}}$, the temperature profile remains relatively uniform with a modest gradient, indicative of limited heat recirculation and reduced matrix temperatures. As the mass flux increases to $\dot{m}'' = 0.19\,\mathrm{kgm^{-2}s^{-1}}$, the temperature gradient steepens significantly, reflecting enhanced thermal feedback and greater heat transfer within the ceramic matrix. The exhaust gas temperature, T_g, rises correspondingly from 1314 K to 1445 K, with the thermal load increasing by 1.3 kW. At the highest mass flux tested, $\dot{m}'' = 0.25$ $\mathrm{kgm^{-2}s^{-1}}$, the trend of augmented peak temperatures continues, reaching up to 1560 K, along with more pronounced temperature gradients.

In summary, the combined analysis of solid matrix temperature distributions and their averaged profiles under varying equivalence ratios, fuel compositions, and mass flux conditions portrays the adaptability of porous media to stabilize the flame. In the present configuration, there appears to be a narrow range of flame stabilization locations, in between r = 12 and 18 mm, in which variations in flame speed or mass flux are dynamically balanced by the velocity gradient induced by the radially inward flow geometry

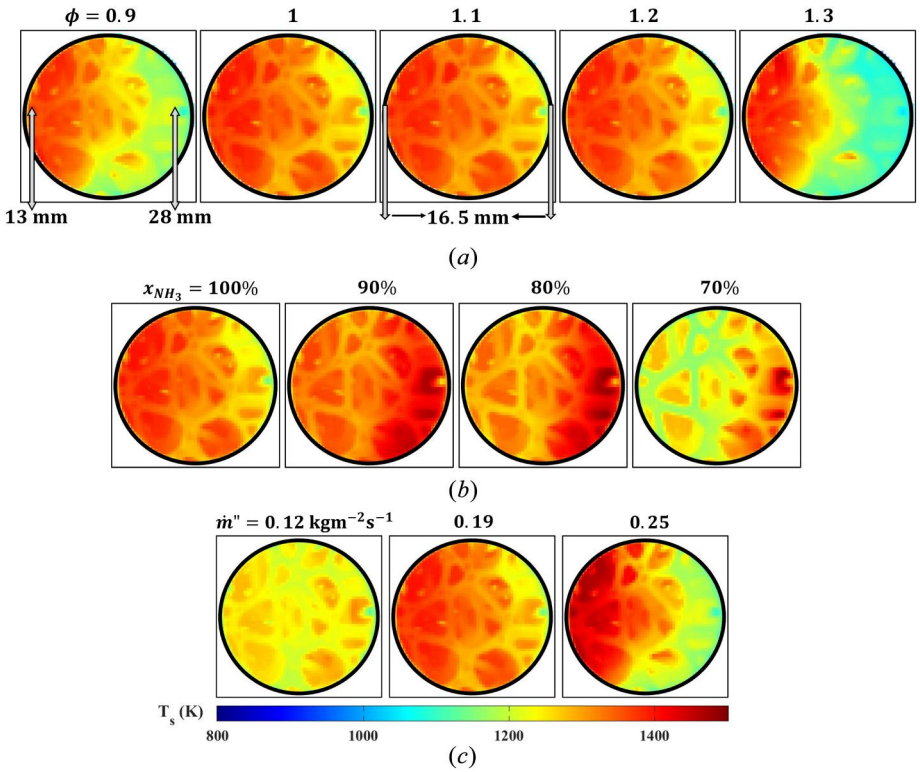

Fig. 7 Solid matrix temperature distribution across the porous media as a function of equivalence ratio ϕ, volumetric fraction x_{NH_3}, and mass flux $\dot{m}''$: (*a*) $x_{NH_3} = 100\%$ and $\dot{m}'' = 0.19$ kgm^{-2}s^{-1}, (*b*) $\dot{m}'' = 0.19$ kgm^{-2}s^{-1} and $\varphi = 1$, and (*c*) $x_{NH_3} = 100\%$ and $\varphi = 1$

and pore size gradient. Increasing flame speed excessively (e.g., by high H_2 content) leads to a partial flashback and re-establishes the flame in a narrow region outside of the porous matrix at the outer circumference of the burner. Excessive mass flux pushes the flame downstream out of the stability range for pure ammonia operation at $\dot{m}'' > 0.25$ kgm^{-2}s^{-1}.

3.3 Pollutant Emissions. Figure 9 presents the measured NO, N_2O, H_2, and NH_3 in the exhaust gas as a function of ϕ for $x_{NH_3} = 100\%$, 90%, 80%, and 70% and a fixed mass flux of $\dot{m}'' = 0.19$ kgm^{-2}s^{-1}. The exhaust NO emissions were reported dry and normalized to 15% O_2 concentration, following standard practices for emissions measurements of gas turbine combustors [50]. Consistent with previous studies on porous media combustion of NH_3 [34,35], high NO levels were recorded for flames close to stoichiometric conditions and increased with growing H_2 content in the NH_3 fuel mixture. NO emissions were significantly reduced for the rich mixtures ($\phi \geq 1.2$) and also decreased linearly with decreasing equivalence ratio under lean conditions. A 30% increase in H_2 addition from $x_{NH_3} = 100$–70% yields an increase in NO emission by 60% for stoichiometry operation, peaking at 3200 ppmv. The high NO levels were correlated to the conditions that led to flame location being furthest upstream, as was the case for high H_2 content mixtures seen in Fig. 8(*b*). This allows for long residence time at high temperatures, which is correlated to high NO emissions in ammonia combustion. However, the measured N_2O emissions increase substantially under very lean conditions ($\phi \leq 0.6$), as shown in Fig. 9(*b*), consistent with previous findings [18,51]. Minimal N_2O emissions were observed for $\phi \geq 0.8$ across all

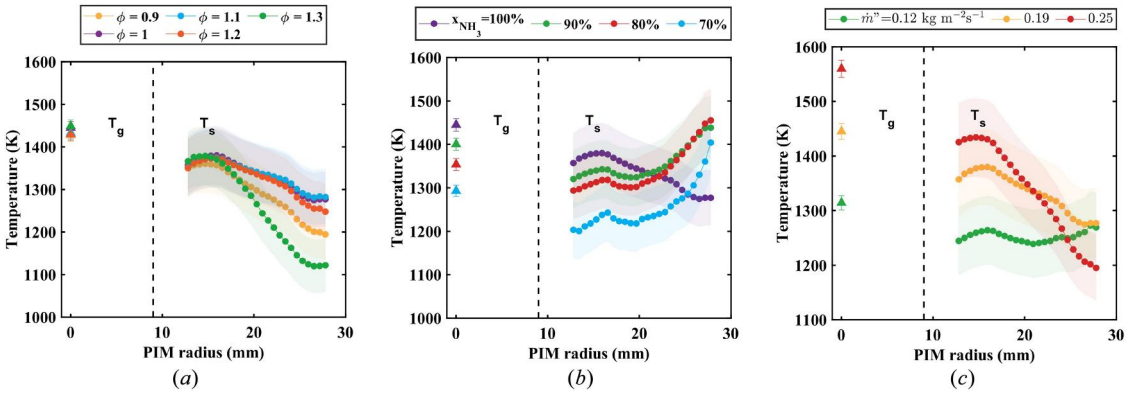

Fig. 8 Radial profiles of solid matrix temperature T_s as functions of equivalence ratio ϕ, volumetric fraction x_{NH_3}, and mass flux $\dot{m}''$. Measured exhaust gas temperature T_g is shown relative to the PIM radius. (*a*) $x_{NH_3} = 100\%$ and $\dot{m}'' = 0.19$ kgm^{-2}s^{-1}, (*b*) $\dot{m}'' = 0.19$ kgm^{-2}s^{-1} and $\varphi = 1$, and (*c*) $x_{NH_3} = 100\%$ and $\varphi = 1$.

mixtures (N_2O emissions were calibrated down to 150 ppm), while a peak value of 1700 ppmv was recorded at $\phi = 0.5$ for $x_{NH_3} = 70\%$. For $x_{NH_3} = 100\%$, the N_2O concentration remained below 150 ppm at all stable equivalence ratios ($0.9 \leq \phi \leq 1$) for the present mass flux rate. N_2O emissions are primarily attributed to low temperature operation under these conditions, which promotes N_2O survival. Furthermore, N_2O emissions increase with NH_3 content, suggesting that lower temperatures along with increased fuel-bound N favor N_2O accumulation. This trend aligns with observed NO emission reduction under lean conditions (Fig. 9(*a*)), while N_2O formation exhibits an increasing trend, highlighting the interplay between these two emissions with the combustion temperature.

Figures 9(*c*) and 9(*d*) show the volumetric measurements of unburned H_2 and NH_3 in rich mixtures ($\phi \geq 1$) with different compositions of NH_3/H_2. Rich NH_3 combustion is known to produce a significant amount of unburned reactants, mainly in the form of NH_3 and H_2, with a large fraction appearing as H_2 slip. Unburned NH_3 increases with ϕ in all mixtures, reaching 1% in pure NH_3 combustion at $\phi = 1.3$ and slightly greater in $x_{NH_3} = 80\%$ and 90% mixtures at $\phi = 1.4$. The increase in unburned levels of NH_3, reflects the challenge of achieving low NO_x and low NH_3 slip operation under fuel-rich conditions. H_2 emissions also increase with ϕ for all mixtures. This is particularly noticeable in the mixtures with higher contents of H_2, such as $x_{NH_3} = 70\%$ case, where the volumetric fraction of the H_2 slip gradually increased to 12%. For these conditions, the opportunity for second-stage combustion arises, as was demonstrated in PMBs by Vignat et al. [38].

A comparison between the experimental measurements (dashed lines) and the predictions of a simple perfectly stirred reactor (PSR) model for NO, N_2O, H_2, and NH_3 emissions is also presented in Fig. 9. The PSR model was implemented in Cantera [52] and used the kinetic model of Stagni et al. [53]. The PSR model was applied under approximated experimental conditions, with the residence time corresponding to mass flux. To compensate for heat loss to the ceramic matrix, the model assumed a temperature that was 150 K lower than the adiabatic flame temperature for each respective NH_3/H_2 mixture, resulting in optimized matches to the experimental data. The model shows a good qualitative agreement in predicting NO, H_2, and NH_3 emissions in a range of equivalence ratios ϕ. A significant deviation between the model and the experimental results was observed near the peak NO emissions, likely due to the limitations of the simple model to account for significant changes in flame location apparent at these conditions, see Fig. 8. However, N_2O predictions from the PSR model using Stagni et al. [53] reaction mechanism overestimates N_2O levels, whereas Nakamura et al. [54] show better agreement with the experiments of $x_{NH_3} = 70\%$ case in

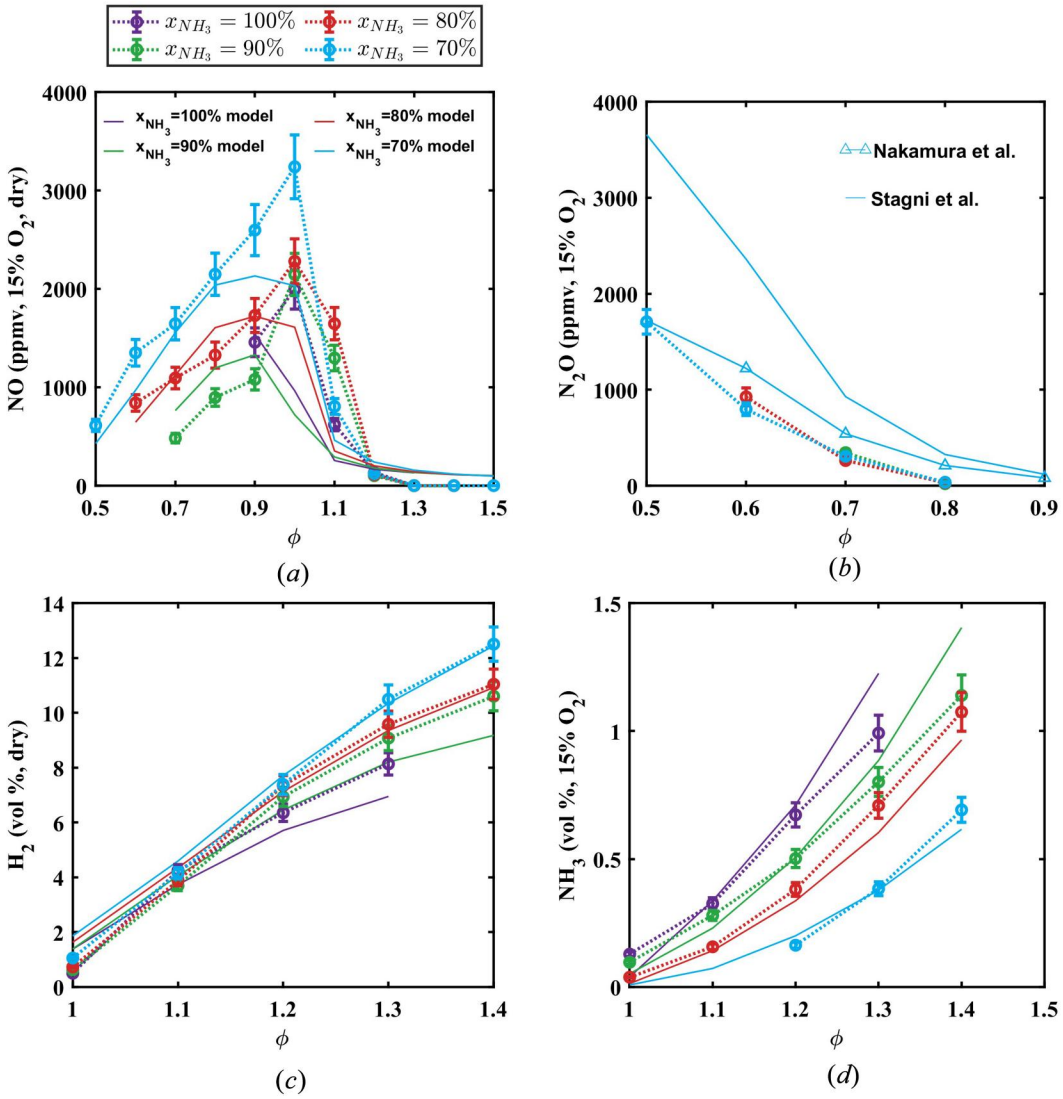

Fig. 9 Measurements of NO, N_2O, H_2, and NH_3 as a function of x_{NH_3} and the equivalence ratio ϕ, for a mass flux of $\dot{m}'' = 0.19$ kgm^{-2}s^{-1}. The solid lines represent the PSR model predictions. (*a*) Pollutant NO. (*b*) Pollutant N_2O. (*c*) Unburned H_2. (*d*) Unburned NH_3.

Fig. 9(*b*). The influence of combustion temperature on the formation of NO, H_3, and NH_3 slip is presented in Appendix B.

Following previous studies [4,53,55–60], analysis of the model shows that the consumption of NH_3 occurs predominantly through the H abstraction reaction to form NH_2, with hydroxyl radicals (OH) being the main reactants under all equivalence ratios. Secondary fuel consumption reactions involve hydrogen (H) and oxygen (O), though these are less significant than OH in depleting NH_3. The oxidation of NH_i species (where $i = 1$ or 2) has two possible outcomes, depending on the proportion of O/H radicals available. When the O/H ratio is high, NH_i species undergo rapid oxidation to form NO through the HNO intermediate. For a low O/H ratio, NH_2 more gradually converts to NH, eventually forming NO. For rich mixtures, the ratio of O/H is decreased while the overall concentration of H increases. The increase in H radical increases its reaction rate with NH_i to compete with NO production pathways, leading to the observed low NO production [57]. Numerous studies have identified the formation of NO due to fuel-bound NO_x pathways, particularly through intermediates such as HNO, NH_i, and N_2O [60,61]. The formation of N_2O occurs through the reaction of NO with NH. Mashruk et al. [51] provided a detailed analysis on N_2O formation and reduction using reaction pathway analysis and sensitivity coefficients of the reaction mechanism used in this study, identifying the dominant reaction pathways and key factors influencing N_2O emissions. Haynes [62] reported the formation of N_2 through a $NH_i + NH_i$ combination reaction through intermediate species N_2H_2. This mechanism dominates the kinetics of rich ammonia flames and contributes to low NO production. Using a chemical reactor network model, it was demonstrated that the formation of N_2 via a pollutant pathway involves HNO, NO, and N_2O intermediates, and the N_2H_2 pathway, through NNH intermediates [34]. The pollutant pathway was revealed to play an important role in lean conditions, while the N_2H_2 pathway dominates in rich combustion conditions.

The effect of varying the mass flux on the NO emission and the unburned O_2 and H_2 concentrations of the stabilized NH_3 flames is presented in Fig. 10. For lean cases, $0.8 < \phi < 1$, the concentration of NO ranges between 350 and 3000 ppmv (15% O_2) and tends to increase with increasing mass flux. With a twofold increase in mass flux from 0.12 to 0.25 $kgm^{-2}s^{-1}$, NO emissions increased approximately four times under stoichiometric conditions, highlighting the strong dependence of NO formation on mass flux, related to increased combustion temperature (see Figs. 7(*c*) and 8(*c*)). Higher mass fluxes were previously reported in PMBs to improve the reforming of NH_3 [35]. In Fig. 10(*b*), increased $\dot{m}''$ is accompanied by an increase in the unburned volume fraction H_2 across all ϕ values.

The results of Fig. 10(*a*) indicate the lowest amount of NO pollutants occurs near the extinction limits of the PMB, at a mass flux of $\dot{m}'' = 0.12$ $kgm^{-2}s^{-1}$. According to Fig. 10(*c*), combustion

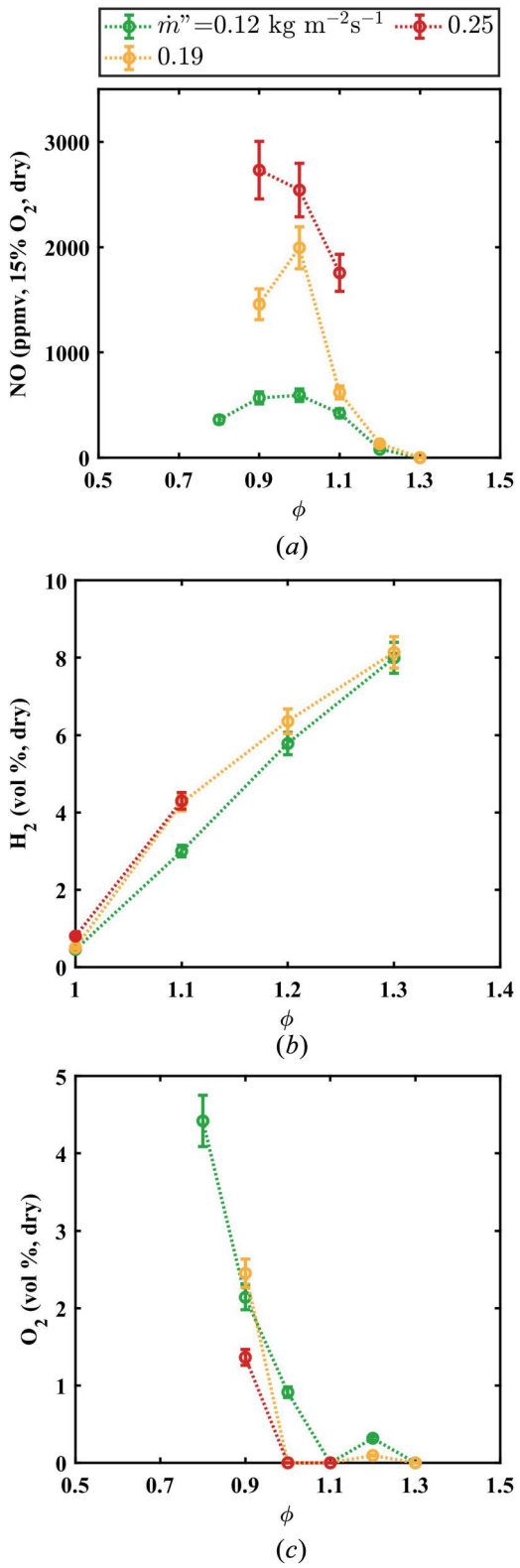

Fig. 10 Effect of mass flux on NO and H_2 emissions, residual O_2 of the burner for the NH_3 combustion: (*a*) pollutant NO, $x_{NH_3} = 100\%$, (*b*) unburned H_2, $x_{NH_3} = 100\%$, and (*c*) residual O_2, $x_{NH_3} = 100\%$

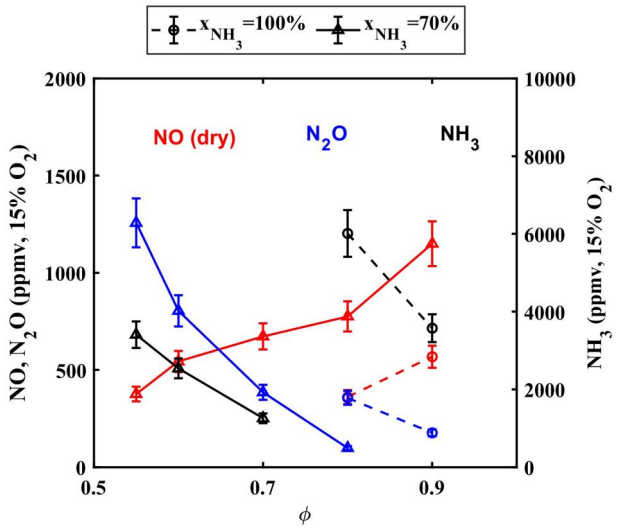

Fig. 11 Measured NO, N_2O, and NH_3 emissions under lean conditions for a mass flux of $\dot{m}'' = 0.12$ $kgm^{-2}s^{-1}$

efficiency was slightly reduced for this case, resulting in approximately 1% of unburned O_2 at stoichiometric conditions, but was comparable to the higher mass flux cases for the $\phi = 0.9$ case. Operation using the near-extinction limit mass flux was often explored in porous media combustion to achieve low NO emissions [34,35]. Figure 11 expands on these conditions, and shows the measured NO, N_2O, and unburned NH_3 (normalized to 15% O_2) for operating conditions with $x_{NH_3} = 100\%$ and $x_{NH_3} = 70\%$ at $\dot{m}'' = 0.12$ kgm^{-2}s^{-1}. For $x_{NH_3} = 100\%$ operation, the extinction limit of the burner is reached at $\phi = 0.8$, where the NO and N_2O emissions were measured to be 360 and 356 ppmv, respectively. Operation at $\phi = 0.9$ increased the NO emissions to 568 ppm and reduced the N_2O emissions to 176 ppm. With H_2 blending, at $x_{NH_3} = 70\%$, the lean extinction limit was reached at $\phi = 0.55$, where NO and N_2O emissions were measured at 376 and 1256 ppmv, respectively. The lower temperature associated with these leaner conditions promotes N_2O formation while simultaneously reducing NO emissions. Notably, axial PMBs operating at mixture fraction of $x_{NH_3} = 70\%$ reported NO emissions in the range of 1000–2500 ppmv at near-lean extinction conditions ($0.55 < \phi < 0.75$), while the present radial PMB exhibits significantly lower NO emissions, ranging from 376–673 ppmv within a similar equivalence ratio range [35]. The unburned concentration of NH_3 found under these conditions is relatively small compared to rich operating conditions, but still significant, measured to be 6010 ppm at the lean extinction limit for $x_{NH_3} = 100\%$ operation and 3410 ppm at the lean extinction limit for $x_{NH_3} = 70\%$ operation. These results indicate lean operation of near-extinction conditions as an optimal regime for high fuel efficiency and relatively low NO and unburned NH_3 emissions, but not optimal considering N_2O emissions. The tradeoff between NO, NH_3 slip, and N_2O emissions is critical; while NO and NH_3 contribute to air pollution and are harmful to human health, N_2O is relatively inert and nontoxic, but has a significant global warming potential of 298 CO_2 equivalent over an 100 year period. In the present burner operating condition corresponding to the maximum measured N_2O emissions ($\dot{m}'' = 0.19$ kgm^{-2}s^{-1}, $x_{NH_3} = 70\%$ and $\phi = 0.5$), the exhaust stream would contain approximately 54% CO_2.

4 Conclusions

This study investigated the combustion of premixed NH_3/H_2/air flames stabilized within a solid porous media matrix. The radial inward flow porous media burner demonstrated effective flame stabilization across various operating conditions. The graded topology of the ceramic foam facilitated the stabilization of the large flame thickness characteristic of NH_3. The compact geometry of the porous media achieved a high volumetric power density compared to conventional PMBs and swirl-stabilized NH_3 flames, making it more suitable for compact power generation applications, particularly in microgas turbines. Infrared radiometry was used to estimate the temperature of the solid matrix for the first time. The dynamic flame stabilization was analyzed in relation to fuel composition, equivalence ratio, and mass flux. The correlation between the estimated solid matrix temperature and the exhaust gas temperature provided insight into flame stabilization mechanisms.

Emission measurements of NO, N_2O, unburned NH_3, and H_2 were conducted. A qualitative comparison was performed with a simple perfectly stirred reactor model using a 150 K lower temperature than predicted by an adiabatic calculation; predicted emission trends closely match the measured emissions of this burner. The observed NO emissions increased as the reactant mixture transitioned from lean to stoichiometric conditions ($\phi \leq 1$) and decreased significantly under rich combustion ($\phi \geq 1.2$). Near the lean extinction limit, NO emissions remained below 670 ppmv with high hydrogen blending ($x_{H_2} = 30\%$). However, N_2O emissions increase substantially at very lean conditions ($\phi \leq 0.6$). For pure NH_3 combustion, low NO levels were observed under near lean extinction limits, while high concentrations of unburned NH_3 in rich conditions were attributed to low combustion temperature. Adding H_2 content to NH_3 fuel extended the flammability limits but led to increased NO levels from lean to stoichiometric conditions and elevated unburned H_2 concentration in rich mixtures. The overall ratio of unburned H_2 to NH_3 increased with fuel richness and a higher H_2 content. Additionally, increased heat recirculation with higher mass flux led to elevated NO levels and unburned H_2 volume fractions.

This study identified regimes for low NO emissions: a) near lean-limit NH_3/H_2 combustion, where a tradeoff with increased N_2O formation is observed, b) under rich conditions of $\phi \geq 1.2$, and c) for pure NH_3 at low combustion temperature associated with low mass flux. Advancements in additive manufacturing offer opportunities to optimize the pore size for extended flame stabilization in NH_3/air flames. The PMB of the radial inward flow shows potential as a practical solution for NH_3 fueled microgas turbines.

Acknowledgment

The authors thank Alex Kleiman, Yohai Abraham, Gabriel Shamai, Anton Agapovichev, David Peles, and Max Bernard for their help in the experimental campaigns.

Funding Data

- Israeli Ministry of Energy (Contract No. 221-11-063).
- Minerva Research Center, Max Planck Society (Contract No. AZ5746940764; Funder ID: 10.13039/501100001658).

Data Availability Statement

The datasets generated and supporting the findings of this article are obtainable from the corresponding authors upon reasonable request.

Nomenclature

L = foam thickness (mm)
$\dot{m}''$ = mass flux (kgm^{-2}s^{-1})
P_o = atmospheric pressure (Pa)
$\dot{q}_v$ = thermal power density (MW m^{-3})
T_g = exhaust gas temperature (K)
T_s = solid matrix temperature (K)
x_{H_2} = volumetric fraction of H_2
x_{NH_3} = volumetric fraction of NH_3
z = axial distance across foam (mm)
$\Delta = P$ = pressure drop (Pa)

Abbreviations

PIM = porous inert media
PMB = porous media burner
PSR = perfectly stirred reactor
SiC = silicon carbide

Greek Symbols

ε = emissivity
ϕ = equivalence ratio

Superscripts and Subscripts

g = gaseous
s = solid
v = volume

Appendix A: Estimated Radiation Heat Loss

To estimate radiation heat losses, this study used simple 0D formulations to characterize two-body radiation heat transfer [63]. The radiative heat loss fraction (fraction of total heat input that is lost via radiation) is systematically evaluated in both directions of the solid matrix for different solid temperatures in Fig. S1 available in the Supplemental Materials on the ASME Digital Collection. Considering a heat input (Q_{in}) based on a

mass flux of $\dot{m}'' = 0.19\,\mathrm{kgm^{-2}s^{-1}}$, the radiative heat loss fraction is found to be approximately 10% for solid matrix temperatures observed between 1300 to 1400 K in NH_3 combustion. The dominant direction of radiation loss depends on the flame stabilization location. When the flame stabilizes near the upstream, radial radiation loss dominates, and conversely, flame stabilization within the porous matrix results in higher axial radiation losses.

Appendix B: Effect of Combustion Temperature on the Formation of NO, H_2, and NH_3 Slip

The PSR model provides a valid approach for evaluating the effects of temperature variations on emissions formation using Stagni et al. [53] mechanism. To systematically assess the influence of heat losses on pollutant formation, the model assumes reduced flame temperatures ΔT $(=T_{ad} - T)$ of 150 and 300 K. However, it is important to note that these imposed temperature reductions are specific to the modeling approach, whereas actual temperature drops in an experimental system depends on multiple factors such as flow conditions, matrix temperature, and external cooling effects. The PSR model predictions in Fig. S2 available in the Supplemental Materials demonstrate the role of combustion temperature in the formation of NO emissions in the system. The agreement between measured emissions and PSR predictions for $\Delta T = 150$ supports the conclusion that heat loss influences pollutant formation, leading to a 40% reduction in NO emission at stoichiometric conditions relative to adiabatic conditions $(\Delta T = 0)$ in Fig. S2(a) available in the Supplemental Materials. Furthermore, elevated temperatures promote greater H_2 production and increased NH_3 conversion, thereby reducing unburned NH_3 slip (refer to Figs. S2(b) and S2(c) available in the Supplemental Materials). However, this effect simultaneously leads to elevated NO formation in lean conditions, emphasizing the need to balance temperature, equivalence ratio, and heat losses to optimize NH_3 combustion performance and emission control.

References

[1] Christoff, P., 2018, "The Promissory Note: COP 21 and the Paris Climate Agreement," *The New Power Politics of Global Climate Governance*, Routledge, Abingdon, UK, pp. 21–43.

[2] Elishav, O., Lis, B. M., Miller, E. M., Arent, D. J., Valera-Medina, A., Dana, A. G., Shter, G. E., and Grader, G. S., 2020, "Progress and Prospective of Nitrogen-Based Alternative Fuels," Chem. Rev., **120**(12), pp. 5352–5436.

[3] Sharma, S., and Ghoshal, S. K., 2015, "Hydrogen the Future Transportation Fuel: From Production to Applications," Renewable Sustainable Energy Rev., **43**, pp. 1151–1158.

[4] Kobayashi, H., Hayakawa, A., Somarathne, K. D. K. A., and Okafor, E. C., 2019, "Science and Technology of Ammonia Combustion," Proc. Combust. Inst., **37**(1), pp. 109–133.

[5] Zamfirescu, C., and Dincer, I., 2008, "Using Ammonia as a Sustainable Fuel," J. Power Sources, **185**(1), pp. 459–465.

[6] Elbaz, A. M., Wang, S., Guiberti, T. F., and Roberts, W. L., 2022, "Review on the Recent Advances on Ammonia Combustion From the Fundamentals to the Applications," Fuel Commun., **10**, p. 100053.

[7] Valera-Medina, A., Vigueras-Zuniga, M. O., Shi, H., Mashruk, S., Alnajideen, M., Alnasif, A., Davies, J., et al., 2024, "Ammonia Combustion in Furnaces: A Review," Int. J. Hydrogen Energy, **49**, pp. 1597–1618.

[8] Kang, L., Pan, W., Zhang, J., Wang, W., and Tang, C., 2023, "A Review on Ammonia Blends Combustion for Industrial Applications," Fuel, **332**, p. 126150.

[9] Valera-Medina, A., Xiao, H., Owen-Jones, M., David, W. I. F., and Bowen, P. J., 2018, "Ammonia for Power," Prog. Energy Combust. Sci., **69**, pp. 63–102.

[10] Li, J., Lai, S., Chen, D., Wu, R., Kobayashi, N., Deng, L., and Huang, H., 2021, "A Review on Combustion Characteristics of Ammonia as a Carbon-Free Fuel," Front. Energy Res., **9**, p. 760356.

[11] Pochet, M., Dias, V., Moreau, B., Foucher, F., Jeanmart, H., and Contino, F., 2019, "Experimental and Numerical Study, Under LTC Conditions, of Ammonia Ignition Delay With and Without Hydrogen Addition," Proc. Combust. Inst., **37**(1), pp. 621–629.

[12] Hayakawa, A., Goto, T., Mimoto, R., Arakawa, Y., Kudo, T., and Kobayashi, H., 2015, "Laminar Burning Velocity and Markstein Length of Ammonia/Air Premixed Flames at Various Pressures," Fuel, **159**, pp. 98–106.

[13] Lee, J. H., Lee, S. I., and Kwon, O. C., 2010, "Effects of Ammonia Substitution on Hydrogen/Air Flame Propagation and Emissions," Int. J. Hydrogen Energy, **35**(20), pp. 11332–11341.

[14] Karan, A., Dayma, G., Chauveau, C., and Halter, F., 2022, "Experimental Study and Numerical Validation of Oxy-Ammonia Combustion at Elevated Temperatures and Pressures," Combust. Flame, **236**, p. 111819.

[15] Pugh, D., Runyon, J., Bowen, P., Giles, A., Valera-Medina, A., Marsh, R., Goktepe, B., and Hewlett, S., 2021, "An Investigation of Ammonia Primary Flame Combustor Concepts for Emissions Reduction With OH*, NH_2* and NH* Chemiluminescence at Elevated Conditions," Proc. Combust. Inst., **38**(4), pp. 6451–6459.

[16] Hayakawa, A., Arakawa, Y., Mimoto, R., Somarathne, K. D. K. A., Kudo, T., and Kobayashi, H., 2017, "Experimental Investigation of Stabilization and Emission Characteristics of Ammonia/Air Premixed Flames in a Swirl Combustor," Int. J. Hydrogen Energy, **42**(19), pp. 14010–14018.

[17] Khateeb, A. A., Guiberti, T. F., Zhu, X., Younes, M., Jamal, A., and Roberts, W. L., 2020, "Stability Limits and NO Emissions of Technically-Premixed Ammonia-Hydrogen-Nitrogen-Air Swirl Flames," Int. J. Hydrogen Energy, **45**(41), pp. 22008–22018.

[18] Mashruk, S., Vigueras-Zuniga, M. O., del Cueto, M.-E. T., Xiao, H., Yu, C., Maas, U., and Valera-Medina, A., 2022, "Combustion Features of $CH_4/NH_3/H_2$ Ternary Blends," Int. J. Hydrogen Energy, **47**(70), pp. 30315–30327.

[19] Ahmed, M. M. A., Xu, L., Bai, X.-S., Hassan, Z. O., Abdullah, M., Sim, J., Cenker, E., Roberts, W. L., and Elbaz, A. M., 2024, "Flame Stabilization and Pollutant Emissions of Turbulent Ammonia and Blended Ammonia Flames: A Review of the Recent Experimental and Numerical Advances," Fuel Commun., **20**, p. 100127.

[20] Božo, M. G., Vigueras-Zuniga, M. O., Buffi, M., Seljak, T., and Valera-Medina, A., 2019, "Fuel Rich Ammonia–Hydrogen Injection for Humidified Gas Turbines," Appl. Energy, **251**, p. 113334.

[21] Franco, M. C., Rocha, R. C., Costa, M., and Yehia, M., 2021, "Characteristics of NH_3/H_2/Air Flames in a Combustor Fired by a Swirl and Bluff-Body Stabilized Burner," Proc. Combust. Inst., **38**(4), pp. 5129–5138.

[22] Zhu, X., Khateeb, A. A., Guiberti, T. F., and Roberts, W. L., 2021, "NO and OH* Emission Characteristics of Very-Lean to Stoichiometric Ammonia–Hydrogen–Air Swirl Flames," Proc. Combust. Inst., **38**(4), pp. 5155–5162.

[23] Cai, T., Zhao, D., and Gutmark, E., 2023, "Overview of Fundamental Kinetic Mechanisms and Emission Mitigation in Ammonia Combustion," Chem. Eng. J., **458**, p. 141391.

[24] Valera-Medina, A., Pugh, D. G., Marsh, P., Bulat, G., and Bowen, P., 2017, "Preliminary Study on Lean Premixed Combustion of Ammonia–Hydrogen for Swirling Gas Turbine Combustors," Int. J. Hydrogen Energy, **42**(38), pp. 24495–24503.

[25] Mashruk, S., Okafor, E. C., Kovaleva, M., Alnasif, A., Pugh, D., Hayakawa, A., and Valera-Medina, A., 2022, "Evolution of N_2O Production at Lean Combustion Condition in NH_3/H_2/Air Premixed Swirling Flames," Combust. Flame, **244**, p. 112299.

[26] Khateeb, A. A., Guiberti, T. F., Zhu, X., Younes, M., Jamal, A., and Roberts, W. L., 2020, "Stability Limits and Exhaust NO Performances of Ammonia–Methane–Air Swirl Flames," Exp. Therm. Fluid Sci., **114**, p. 110058.

[27] Wood, S., and Harris, A. T., 2008, "Porous Burners for Lean-Burn Applications," Prog. Energy Combust. Sci., **34**(5), pp. 667–684.

[28] Mujeebu, M. A., Abdullah, M. Z., Bakar, M. Z. A., Mohamad, A. A., Muhad, R. M. N., and Abdullah, M. K., 2009, "Combustion in Porous Media and Its Applications–A Comprehensive Survey," J. Environ. Manage., **90**(8), pp. 2287–2312.

[29] Pereira, F. M., Oliveira, A. A. M., and Fachini, F. F., 2011, "Maximum Superadiabatic Temperature for Stabilized Flames Within Porous Inert Media," Combust. Flame, **158**(11), pp. 2283–2288.

[30] Howell, J. R., Hall, M. J., and Ellzey, J. L., 1996, "Combustion of Hydrocarbon Fuels Within Porous Inert Media," Prog. Energy Combust. Sci., **22**(2), pp. 121–145.

[31] Masset, P.-A., Dounia, O., and Selle, L., 2021, "Fully Explicit Formulae for Flame Speed in Infinite and Finite Porous Media," Combust. Theory Modell., **25**(5), pp. 785–812.

[32] Nozari, H., Karaca, G., Tuncer, O., and Karabeyoglu, A., 2017, "Porous Medium Based Burner for Efficient and Clean Combustion of Ammonia–Hydrogen–Air Systems," Int. J. Hydrogen Energy, **42**(21), pp. 14775–14785.

[33] Rocha, R. C., Ramos, C. F., Costa, M., and Bai, X.-S., 2019, "Combustion of NH_3/CH_4/Air and NH_3/H_2/Air Mixtures in a Porous Burner: Experiments and Kinetic Modeling," Energy Fuels, **33**(12), pp. 12767–12780.

[34] Vignat, G., Akoush, B., Toro, E. R., Boigné, E., and Ihme, M., 2022, "Combustion of Lean Ammonia–Hydrogen Fuel Blends in a Porous Media Burner," Proc. Combust. Inst., **39**(4), pp. 4195–4204..

[35] Vignat, G., Zirwes, T., Toro, E. R., Younes, K., Boigné, E., Muhunthan, P., Simitz, L., Trimis, D., and Ihme, M., 2023, "Experimental and Numerical Investigation of Flame Stabilization and Pollutant Formation in Matrix Stabilized Ammonia–Hydrogen," Combust. Flame, **250**, p. 112642.

[36] Chen, D., Li, J., Li, X., Deng, L., He, Z., Huang, H., and Kobayashi, N., 2023, "Study on Combustion Characteristics of Hydrogen Addition on Ammonia Flame at a Porous Burner," Energy, **263**, p. 125613.

[37] Zirwes, T., Vignat, G., Toro, E. R., Boigné, E., Younes, K., Trimis, D., and Ihme, M., 2023, "Improving Volume-Averaged Simulations of Matrix-Stabilized Combustion Through Direct X-Ray μCT Characterization: Application to NH_3/H_2-Air Combustion," Combust. Flame, **257**, p. 113020.

[38] Vignat, G., Zirwes, T., Boigné, É., and Ihme, M., 2024, "Experimental Demonstration of a Two-Stage Porous Media Burner for Low-Emission Ammonia Combustion," Proc. Combust. Inst., **40**(1–4), p. 105491.

[39] Noordally, E., Przybylski, J. M., and Witton, J. J., 2004, "Porous Media Combustors for Clean Gas Turbine Engines," Cranfield University, United Kingdom, Report No. ADA429816, pp. 1–45.

[40] Mohaddes, D., Chang, C. T., and Ihme, M., 2020, "Thermodynamic Cycle Analysis of Superadiabatic Matrix-Stabilized Combustion for Gas Turbine Engines," Energy, **207**, p. 118171.
[41] Badum, L., Leizeronok, B., and Cukurel, B., 2021, "New Insights From Conceptual Design of an Additive Manufactured 300 W Microgas Turbine Toward Unmanned Aerial Vehicle Applications," ASME J. Eng. Gas Turbines Power, **143**(2), p. 021006.
[42] Romm, I., and Cukurel, B., 2018, "Quantitative Image Fusion in Infrared Radiometry," Meas. Sci. Technol., **29**(5), p. 055403.
[43] Cagran, C. P., Hanssen, L. M., Noorma, M., Gura, A. V., and Mekhontsev, S. N., 2007, "Temperature-Resolved Infrared Spectral Emissivity of SiC and Pt–10Rh for Temperatures Up to 900 °C," Int. J. Thermophys., **28**(2), pp. 581–597.
[44] Neuer, G., and Jaroma-Weiland, G., 1998, "Spectral and Total Emissivity of High-Temperature Materials," Int. J. Thermophys., **19**(3), pp. 917–929.
[45] Zolotarev, V. M., 2007, "High-Temperature Spectral Emissivity of SiC in the IR Range," Opt. Spectrosc., **103**(4), pp. 592–602.
[46] Hatzl, S., Kirschner, M., Lippig, V., Sander, T., Mundt, C., and Pfitzner, M., 2013, "Direct Measurements of Infrared Normal Spectral Emissivity of Solid Materials for High-Temperature Applications," Int. J. Thermophys., **34**(11), pp. 2089–2101.
[47] Chalia, S., Naagar, M., Thakur, P., Thakur, A., and Sridhara, S. N., 2021, "An Overview of Ceramic Materials and Their Composites in Porous Media Burner Applications," Ceram. Int., **47**(8), pp. 10426–10441.
[48] Pelanconi, M., Rezaei, E., and Ortona, A., 2020, "Cellular Ceramic Architectures Produced by Hybrid Additive Manufacturing: A Review on the Evolution of Their Design," J. Ceram. Soc. Jpn., **128**(9), pp. 595–604.
[49] Valera-Medina, A., Gutesa, M., Xiao, H., Pugh, D., Giles, A., Goktepe, B., Marsh, R., and Bowen, P., 2019, "Premixed Ammonia/Hydrogen Swirl Combustion Under Rich Fuel Conditions for Gas Turbines Operation," Int. J. Hydrogen Energy, **44**(16), pp. 8615–8626.
[50] Baukal, C. E., and Eleazer, P. B., 1998, "Quantifying NO_x for Industrial Combustion Processes," J. Air Waste Manage. Assoc., **48**(1), pp. 52–58.
[51] Mashruk, S., Kovaleva, M., Alnasif, A., Chong, C. T., Hayakawa, A., Okafor, E. C., and Valera-Medina, A., 2022, "Nitrogen Oxide Emissions Analyses in Ammonia/Hydrogen/Air Premixed Swirling Flames," Energy, **260**, p. 125183.
[52] Goodwin, D. G., Moffat, H. K., and Speth, R. L., 2018, "Cantera: An Object-Oriented Software Toolkit for Chemical Kinetics, Thermodynamics, and Transport Processes," California Institute of Technology, Pasadena, CA, accessed Aug. 28, 2025, http://www.cantera.org
[53] Stagni, A., Cavallotti, C., Arunthanayothin, S., Song, Y., Herbinet, O., Battin-Leclerc, F., and Faravelli, T., 2020, "An Experimental, Theoretical and Kinetic-Modeling Study of the Gas-Phase Oxidation of Ammonia," React. Chem. Eng., **5**(4), pp. 696–711.
[54] Nakamura, H., Hasegawa, S., and Tezuka, T., 2017, "Kinetic Modeling of Ammonia/Air Weak Flames in a Micro Flow Reactor With a Controlled Temperature Profile," Combust. Flame, **185**, pp. 16–27.
[55] Lindstedt, R. P., Lockwood, F. C., and Selim, M. A., 1994, "Detailed Kinetic Modelling of Chemistry and Temperature Effects on Ammonia Oxidation," Combust. Sci. Technol., **99**(4–6), pp. 253–276.
[56] Lindstedt, R. P., and Selim, M. A., 1994, "Reduced Reaction Mechanisms for Ammonia Oxidation in Premixed Laminar Flames," Combust. Sci. Technol., **99**(4–6), pp. 277–298.
[57] Miller, J. A., Smooke, M. D., Green, R. M., and Kee, R. J., 1983, "Kinetic Modeling of the Oxidation of Ammonia in Flames," Combust. Sci. Technol., **34**(1–6), pp. 149–176.
[58] Otomo, J., Koshi, M., Mitsumori, T., Iwasaki, H., and Yamada, K., 2018, "Chemical Kinetic Modeling of Ammonia Oxidation With Improved Reaction Mechanism for Ammonia/Air and Ammonia/Hydrogen/Air Combustion," Int. J. Hydrogen Energy, **43**(5), pp. 3004–3014.
[59] Skreiberg, Ø., Kilpinen, P., and Glarborg, P., 2004, "Ammonia Chemistry Below 1400 K Under Fuel-Rich Conditions in a Flow Reactor," Combust. Flame, **136**(4), pp. 501–518.
[60] Chai, W. S., Bao, Y., Jin, P., Tang, G., and Zhou, L., 2021, "A Review on Ammonia, Ammonia–Hydrogen and Ammonia–Methane Fuels," Renewable Sustainable Energy Rev., **147**, p. 111254.
[61] Alnasif, A., Mashruk, S., Shi, H., Alnajideen, M., Wang, P., Pugh, D., and Valera-Medina, A., 2023, "Evolution of Ammonia Reaction Mechanisms and Modeling Parameters: A Review," Appl. Energy Combust. Sci., **15**, p. 100175.
[62] Haynes, B. S., 1977, "Reactions of Ammonia and Nitric Oxide in the Burnt Gases of Fuel-Rich Hydrocarbon–Air Flames," Combust. Flame, **28**, pp. 81–91.
[63] Badum, L., Schirrecker, F., and Cukurel, B., 2024, "Multidisciplinary Design Methodology for Micro-Gas-Turbines—Part I: Reduced Order Component Design and Modeling," ASME J. Eng. Gas Turbines Power, **146**(10), p. 101001.